




Article

CO₂ Hydrogenation to Methanol over Ce and Zr Containing UiO-66 and Cu/UiO-66

Michalina Stawowy ¹, Radosław Ciesielski ², Tomasz Maniecki ², Krzysztof Matus ³, Rafał Łużny ¹, Janusz Trawczynski ¹, Joaquin Silvestre-Albero ⁴, and Agata Łamacz ^{1,*}

¹ Department of Chemistry and Technology of Fuels, Wrocław University of Science and Technology, Gdańska 7/9, 50-344 Wrocław, Poland; michalina.stawowy@pwr.edu.pl (M.S.); rafal.luzny@pwr.edu.pl (R.Ł.); janusz.trawczynski@pwr.edu.pl (J.T.)

² Institute of General and Ecological Chemistry, Łódź University of Technology, Żeromskiego 116, 90-924 Łódź, Poland; radoslaw.ciesielski@p.lodz.pl (R.C.); tomasz.maniecki@p.lodz.pl (T.M.)

³ Institute of Engineering Materials and Biomaterials, Silesian University of Technology, Konarskiego 18a, 44-100 Gliwice, Poland; krzysztof.matus@polsl.pl

⁴ Laboratorio de Materiales Avanzados, Departamento de Química Inorgánica-IUMA, Universidad de Alicante, Ctra. San Vicente-Alicante s/n, E-03690 San Vicente del Raspeig, Spain; joaquin.silvestre@ua.es

* Correspondence: agata.lamacz@pwr.edu.pl

Received: 3 December 2019; Accepted: 24 December 2019; Published: 30 December 2019

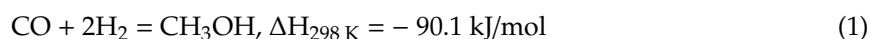


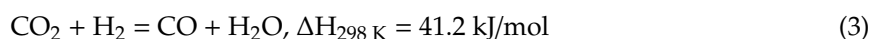
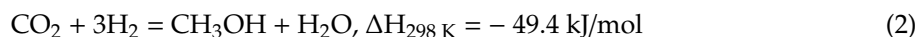
Abstract: Direct hydrogenation of CO₂ to methanol is an interesting method to recycle CO₂ emitted e.g., during combustion of fossil fuels. However, it is a challenging process because both the selectivity to methanol and its production are low. The metal-organic frameworks are relatively new class of materials with a potential to be used as catalysts or catalysts supports, also in the reaction of MeOH production. Among many interesting structures, the UiO-66 draws significant attention owing to its chemical and thermal stability, developed surface area, and the possibility of tuning its properties e.g., by exchanging the zirconium in the nodes to other metal cations. In this work we discuss—for the first time—the performance of Cu supported on UiO-66(Ce/Zr) in CO₂ hydrogenation to MeOH. We show the impact of the composition of UiO-66-based catalysts, and the character of Cu-Zr and Cu-Ce interactions on MeOH production and MeOH selectivity during test carried out for 25 h at T = 200 °C and p = 1.8 MPa. Significant increase of selectivity to MeOH was noticed after exchanging half of Zr⁴⁺ cations with Ce⁴⁺; however, no change in MeOH production occurred. It was found that the Cu-Ce coexistence in the UiO-66-based catalytic system reduced the selectivity to MeOH when compared to Cu/UiO-66(Zr), which was ascribed to lower concentration of Cu⁰ active sites in Cu/UiO-66(Ce/Zr), and this was caused by oxygen spill-over between Cu⁰ and Ce⁴⁺, and thus, the oxidation of the former. The impact of reaction conditions on the structure stability of tested catalyst was also determined.

Keywords: UiO-66; cerium; copper; CO₂ hydrogenation; methanol

1. Introduction

Methanol is one of the most valuable chemicals. It is used as a solvent, fuel, or a raw material for the synthesis of other chemicals, such as formaldehyde, acetic acid, methyl methacrylate, dimethyl terephthalate, dimethyl ether, chloromethanes, and others. In conventional process MeOH is produced from synthesis gas via hydrogenation of CO (Equation (1)) and CO₂ (Equation (2)) and the reversed water-gas shift (RWGS) reaction (Equation (3)).





Synthesis of MeOH is an exothermic reaction that leads to the reduction of the number of molecules; therefore, according to the Le Chatelier's principle, the increase of the pressure and decrease of temperature will favor product formation. However, CO₂ is a chemically inert molecule and its activation requires some increase in reaction temperature. The process is usually carried out over Cu/ZnO/Al₂O₃ catalyst at temperatures between 230 and 280 °C and at elevated pressure of 50–120 bar [1–5]. The active site for MeOH production from CO₂ consists of Cu steps decorated with Zn atoms. Copper, when alone, interacts with CO₂ poorly; hence, the presence of Zn is necessary to enhance its adsorption and speed up its conversion to methanol [6].

MeOH production via CO₂ hydrogenation is a challenging process since the selectivity of the reaction is low and a number of unnecessary and undesired by-products is formed. At higher temperatures the CO formation is favored, so the RWGS reaction (Equation (3)) can occur during MeOH synthesis. That reaction consumes hydrogen and lowers alcohol production. Besides, both the MeOH synthesis (Equation (2)) and RWGS reaction (Equation (3)) produce H₂O that leads to catalyst deactivation by inhibiting the active metal [7].

Direct hydrogenation of CO₂ to obtain methanol is an interesting method to recycle the CO₂ produced, e.g., during combustion of fossil fuels; therefore, that reaction has a significant impact when considering the environmental protection approach because it allows to mitigate CO₂ emissions and provide clean energy. Considering CO₂ conversion to other products, the largest is urea production while the second is MeOH synthesis [8]. It is not clear whether CO₂ is converted directly to MeOH or first to CO, which is next hydrogenated to alcohol; however, the isotope labeling experiments showed that CO is not a carbon source for MeOH creation but its role is to provide an active oxidation state of the copper [9]. Nevertheless, it is clear that hydrogenation reaction takes place over Cu⁰ active sites [10].

Catalyst components, such as the support for Cu, or promoters, play a crucial role in MeOH production and reaction selectivity. For example, incorporation of zirconium into the Cu-Zn catalyst promotes the formation of smaller copper particle which leads to better Cu dispersion [11], and prevents Cu agglomeration and sintering during synthesis and reaction, respectively [12]. The increase of methanol production rate was observed when Mn was introduced to Cu/Zn/Zr [13].

Selection of different carriers can also be beneficial. Liang et al. [14] reported that the Pd-Zn catalysts supported over multi-walled carbon nanotubes (MWNTs) revealed 99.6% selectivity to MeOH and a space time yield (STY) of 37.1 mg_{MeOH}/g_{Cu}/h at 250 °C and 3.0 MPa, which was much better than for PdZn/Al₂O₃. The MWNT support provided higher concentration of the surface-active Pd⁰ species associated with formation of methanol. Deerattrakul et al. [15] studied CuZn/rGO catalyst and reported that the one with 10 wt.% CuZn loading had the highest activity in CO₂ hydrogenation. According to their work, after 5 h on stream at 250 °C and 15 bar, the CO₂ conversion was 26%, CH₃OH selectivity was 51%, and ca. 424 mg MeOH was produced. The catalyst retained its structure after test. However, the increase of CuZn loading above 10 wt.% led to agglomeration of the active phase and resulted in a decreased catalytic performance.

The presence of ceria can be beneficial for the catalyst performance in CO₂ hydrogenation to MeOH. The theoretical and experimental evidence for a CO₂ activation on a copper-ceria interface was presented by Graciani et al. [16]. The combination of metal and oxide centres in the Cu-ceria interface provides favourable reaction pathways for the CO₂ hydrogenation to MeOH, other than observed for a Cu-Zn alloy. The authors found out that the active phase in CeO_x/Cu(111) where 20% of Cu was covered with ceria, was Ce₂O₃/Cu(111). The rate of MeOH production over CeO_x/Cu(111) and Cu(111) was found to be about 200 and 14 times, respectively, faster than on Cu/ZnO. The important fact is that CO₂ adsorbs on CeO₂(111) surface to produce strongly bounded carbonate (CO₃²⁻). However, as was observed with the IRRAS, the CO₃²⁻ species adsorbed on CeO_x/Cu(111) were stable only in the reaction conditions. The adsorbed carbonate species that have lower stability than formate species are

better intermediates for methanol formation. Therefore, the addition of CeO_x NPs to Cu is plausible because it leads to the formation of a metal-oxide interface that enables adsorption and activation of CO₂. The reduction of ceria produces Ce³⁺ centres that are active sites for CO₂ adsorption, which is later activated and hydrogenated to yield a carboxyl species (–COOH) that are next decomposed to CO and –OH. In a subsequent step, CO is hydrogenated to MeOH through the following intermediates: formyl (–CHO), formaldehyde (H₂CO), and methoxy (–OCH₃). In this regard, until CO formation, the synthesis of methanol is realized according to the elementary steps of the RWGS. Allam et al. [17] studied the CuO-ZnO-CeO₂ system that revealed 20% CO₂ conversion and 65% selectivity to methanol at 240 °C and ambient pressure.

MeOH synthesis via CO₂ hydrogenation is structure sensitive. The composition and metal-support interactions play a crucial role in catalyst performance. Most Cu-Zn-containing catalysts possess low surface area (about 30 m²/g), which limits their catalytic function in the reaction. Owing to their developed surface area, surface properties (such as pore size, hydrophobicity/hydrophilicity, Lewis or Brønsted acidity/basicity), and remarkable synergism between their constituents metal-organic frameworks, MOFs can overcome some of the flaws of the conventional catalysts for MeOH synthesis. Improved catalytic performance of MOFs can be achieved by doping them with metal nanoparticles. Electronic interactions between metal and MOF in such a hybrid catalysts are significant for their catalytic activity or selectivity.

Rungtaweivoranit et al. [9] studied copper nanocrystals-encapsulated UiO-66, MIL-101, and ZIF-8 in MeOH synthesis via CO₂ hydrogenation at 175 °C and 10 bar. They found out that only Zr containing UiO-66-based catalyst was active. Moreover, they observed that the location of Cu influences the catalytic activity. The Cu encapsulated in UiO-66 revealed two-fold higher activity and enhanced stability than Cu deposited on UiO-66. Better performance of the former was probably due to enhanced metal-support interaction that allowed formation of active Cu sites for CO₂ conversion to MeOH.

An et al. [18] produced in situ ultra-small Cu/ZnO_x nanoparticles in the UiO-bpy cavities under CO₂/H₂. The agglomeration of Cu nanoparticles and phase separation between Cu and ZnO_x was prevented because of Zr₆ SBUs, strong Cu-ZnO_x interaction, and the bpy moieties on the 2,2'-bipyridine-5,5'-dicarboxylate ligands. After 30 min of CO₂ hydrogenation at 250 °C and *p* = 4 MPa, the catalyst showed 7.2% conversion of CO₂ with 100% selectivity to MeOH and production of 1.97 g_{MeOH}/kg_{Cu}/h.

Recently, Kobayashi et al. [19] reported the Cu supported on Zr-UiO-66, Zr-UiO-66-NH₂, Zr-UiO-66-COOH, and Hf-UiO-66 (with a Cu loading ranging from 13 to 19 wt.%) as hybrid catalysts for CO₂ hydrogenation to methanol. They observed that –COOH group in the BDC linker as well as the replacement of Zr⁴⁺ with Hf⁴⁺ had a beneficial effect on MeOH production, which was higher than that of commercially used Cu/ZnO/Al₂O₃. The MeOH production over Zr-UiO-66-COOH and Hf-UiO-66 was ca. 380 μmol/g_{Cu}/h. In addition, the activity of studied MOF-based catalysts was not associated to the amount of defects in the Zr₆-clusters.

The zirconium containing UiO-66 was first reported by Cavka et al. [20] and owing to its thermal and chemical stability as well as easy functionalization [21–23], it attracted attention of many other researchers. The stability of UiO-66 structure explains its wide use in heterogeneous catalysis. It was studied, e.g., in transesterification of triglyceride with methanol [24], sulphide oxidation [25], desulfurization [26], and other reactions [27]. A number of papers concerning catalytic performance of the UiO-66 modified in Zr nodes or the BDC linker, or decorated with metals, was published. For example, the Cu(II)- and Cu⁰-loaded UiO-66-NH₂ hybrids were found to be highly efficient heterogeneous catalysts for oxidation of cyclohexene and hydrogenation of styrene under mild conditions [28].

In this work we discuss the features and the catalytic properties of Cu supported on UiO-66(Zr) and UiO-66(Ce/Zr). Our intention was to exchange half of Zr⁴⁺ ions with Ce⁴⁺ in the UiO-66 structure and combine it with copper to examine—for the first time—the performance of such a system in CO₂ hydrogenation to MeOH.

2. Results and Discussion

2.1. Characterization of UiO-66

Textural properties of UiO-66 and Cu/UiO-66 materials were determined using the N₂ sorption experiments. Figure 1 and Table 1 present the N₂ adsorption–desorption isotherms, pore size distribution, and textural parameters of the obtained UiO-66 and Cu-UiO-66 materials. The courses of N₂ uptake vs. P/P₀ (Figure 1a) indicate type I isotherms which is characteristic for microporous materials. As is shown in Figure 1b, the majority of pores in obtained materials are smaller than 20 Å. From Table 1 it can be seen that the mean pore width ranges from 23.1 to 23.8 Å. The surface area (S_{BET}) of UiO-66(Zr) is 1380 m²/g, which is higher than that reported in [20–23] and similar to [19]. The decrease in S_{BET} to 810 m²/g is observed when part of Zr cations is replaced with cerium. Further S_{BET} decrease occurs after UiO-66 impregnation with copper nitrate. The decrease in S_{BET} of Zr-UiO-66, Hf-UiO-66, Zr-UiO-66-NH₂, and Zr-UiO-66-COOH after impregnation with Cu(OAc)₂ was also reported [7,19].

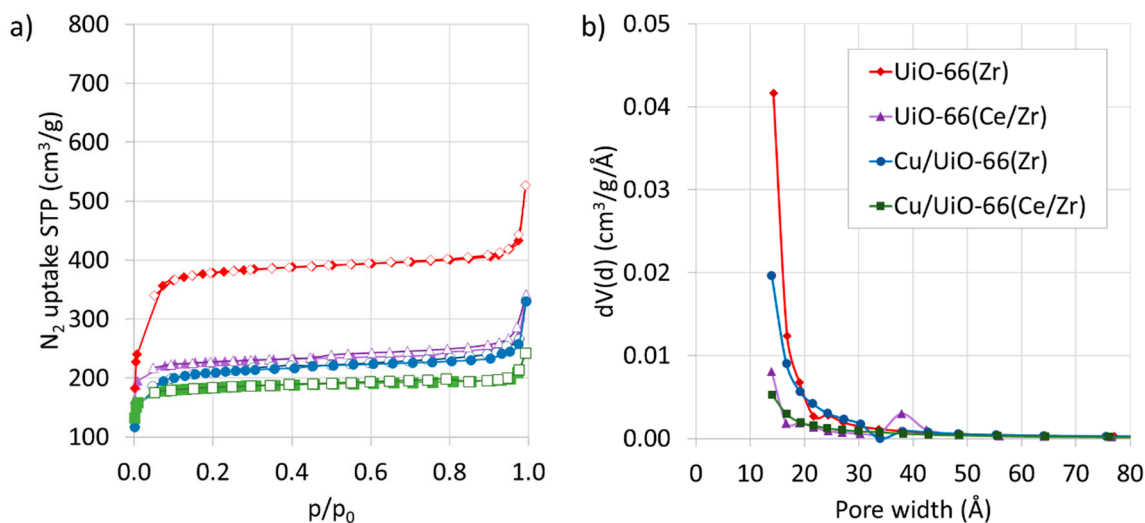


Figure 1. N₂ adsorption isotherms (a) and BJH adsorption pore size distribution (b) for UiO-66 and Cu/UiO-66 materials. In (a) filled symbols—adsorption, empty symbols—desorption.

Table 1. Specific surface area (S_{BET}), total pore volume (V_{total}), and mean pore size (d) for UiO-66 and Cu/UiO-66 materials.

| SAMPLE | S _{BET} (m ² /g) | V _{total} (cm ³ /g) | d (Å) |
|------------------|--------------------------------------|---|-------|
| UiO-66(Zr) | 1380 | 0.545 | 23.5 |
| UiO-66(Ce/Zr) | 810 | 0.373 | 23.1 |
| Cu/UiO-66(Zr) | 757 | 0.507 | 26.8 |
| Cu/UiO-66(Ce/Zr) | 647 | 0.331 | 26.0 |

The crystallographic structures of obtained materials were determined by powder X-ray diffraction (XRD). The XRD patterns of UiO-66 and Cu/UiO-66 materials are presented in Figure 2. It can be observed that all of synthesized materials are crystalline and show sharp reflexes at 2θ of ca. 7.38, 8.52, 12.06, 14.15, and 14.78°, that correspond to reflections for the (111), (200), (220), (311), and (222) planes, respectively. Those reflexes are typical for the UiO-66(Zr) structure [29]. A 1° shift towards lower 2θ is observed for the bimetallic UiO-66(Ce/Zr) which is due to partial replacement of smaller-radii Zr⁴⁺ (0.84 Å) with a bigger-radii Ce⁴⁺ (0.97 Å) [30]. The crystallites sizes calculated from Scherrer equation for the [111] plane were: 31.99 nm for UiO-66(Zr), 52.74 nm for UiO-66(Ce/Zr), 35.17 nm for Cu/UiO-66(Zr), and 63.30 nm for Cu/UiO-66(Ce/Zr). Hence, the Ce introduction to the framework

caused the increase of crystallites size. It is important to note that the crystallinity of the UiO-66(Zr) and UiO-66(Ce/Zr) (Figure 2) was retained after impregnation with copper nitrate. No reflexes coming from Cu phase (Cu, Cu₂O, or CuO) are observed for Cu/UiO-66(Zr) and Cu/UiO-66(Ce/Zr), which can be due to relatively low Cu loading and its good dispersion over the framework.

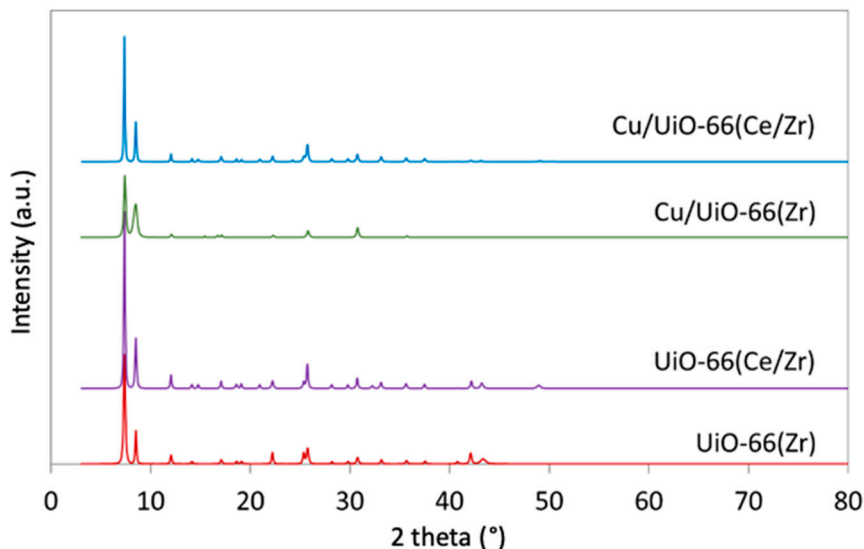


Figure 2. XRD for UiO-66 and Cu/UiO-66 materials.

The X-ray photoelectron spectroscopy (XPS) proved that in Cu/UiO-66(Zr) and Cu/UiO-66(Ce/Zr) samples copper was present both in the form of CuO and Cu₂O. The Cu 2p XPS spectra presented in Figure 3a,c display the Cu 2p_{3/2} and Cu 2p_{1/2} peaks of Cu²⁺ at ca. 934 and 954 eV, respectively, with a strong shake-up satellite at ca. 944 eV [31]. Whereas peaks at ca. 932 and 952 eV correspond to Cu⁺. The Ce 3d spectra for UiO-66(Ce/Zr) and Cu/UiO-66(Ce/Zr) (Figure 3b,d) display several bands attributed to the presence of Ce³⁺ and Ce⁴⁺ cations in the UiO-66 framework. The bands at 903.57, 899.48, 885.26, 880.63 eV are characteristic for cerium in +3 oxidation state, whereas bands at 916.66, 906.69, 900.75, 898.20, 888.38 and 882.31 eV are typical for cerium in +4 oxidation state [32]. The presence of Ce³⁺ ions is important for CO₂ adsorption and activation. The theoretical concentration of Zr in UiO-66 is 6.97 At.% (33.49 wt.%), whereas the concentration of Ce and Zr in UiO-66(Ce/Zr), when Ce:Zr is 1:1, should be 3.48 At.% for each metal (i.e., 15.36 wt.% for Zr and 23.59 wt.% for Ce). It was calculated that the concentration of Ce in UiO-66(Ce/Zr) and Cu/UiO-66(Ce/Zr) was 2.78 and 2.51 At.%, which is lower than the theoretical value. The Ce⁴⁺/Ce³⁺ ratio was 1.63 and 1.53, respectively. Hence, the Ce⁴⁺ predominated over Ce³⁺. The increase of Ce³⁺ by the cost of Ce⁴⁺ in Cu/UiO-66(Ce/Zr) can be due to oxygen transfer at the Cu⁺–Ce⁴⁺ interface, thus leading to the reduction of Ce⁴⁺ to Ce³⁺.

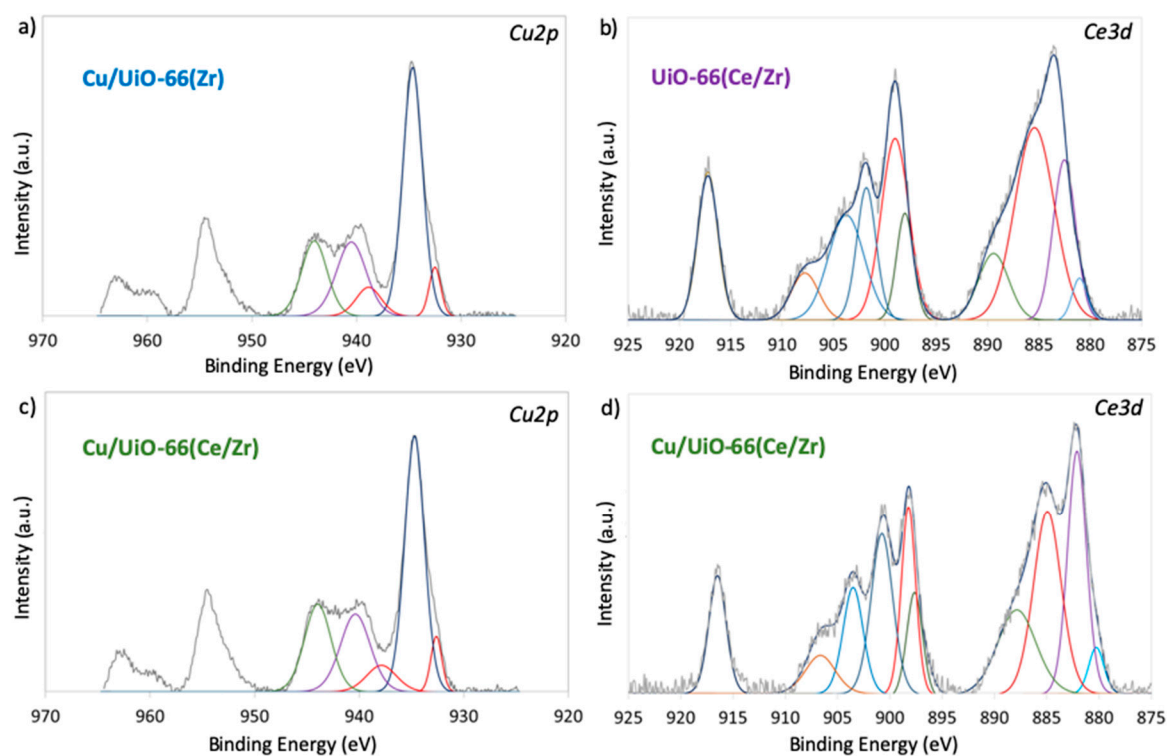


Figure 3. Cu2p and Ce3d X-ray photoelectron spectroscopy (XPS) spectra for Cu/UIO-66(Zr) (a), UiO-66(Ce/Zr) (b), and Cu/UIO-66(Ce/Zr) (c,d).

Determination of the morphology of the obtained materials and distribution of particular metals within and over the UiO-66 framework was performed with scanning electron microscope (SEM) and high-resolution transmission electron microscope (HRTEM). The elemental composition of the obtained in this work UiO-66(Ce/Zr) is presented in Table 2, displaying lower than assumed concentration of Ce. It proves that less than 50% of Zr^{4+} was replaced with Ce^{4+} . It is important to notice that mapping of the UiO-66(Ce/Zr) (Figure 4) showed uniform dispersion of Ce and Zr in the sample.

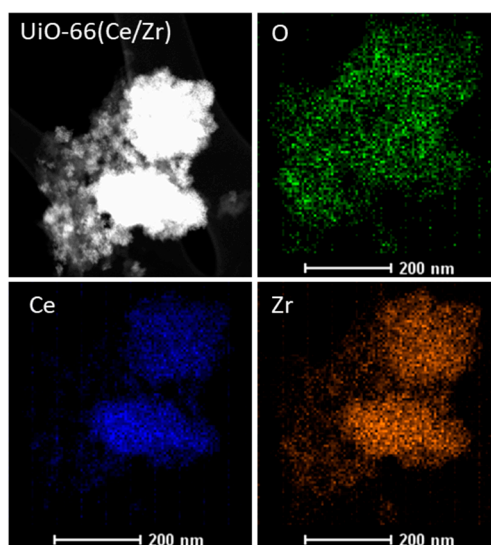
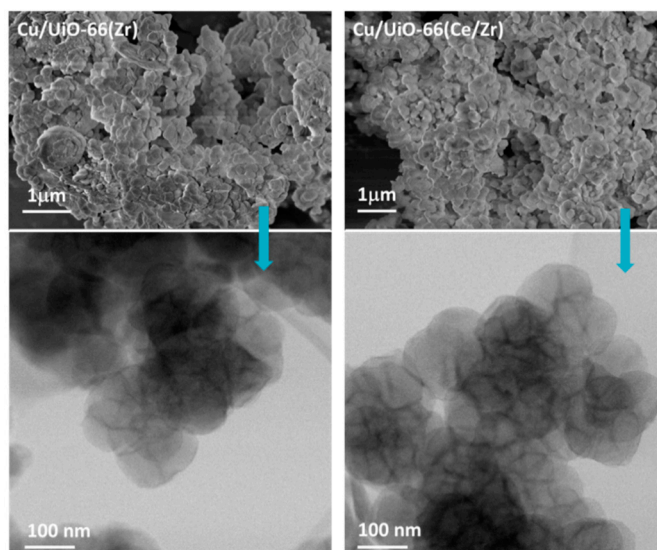
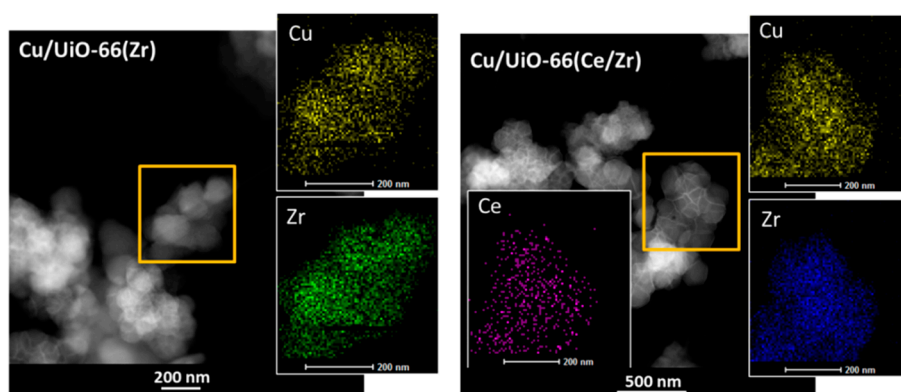


Figure 4. Scanning transmission electron microscopy (STEM) image of UiO-66(Ce/Zr) with energy dispersive X-ray spectroscopy (EDS) maps of Ce, Zr, and O.

Table 2. Elemental composition of the UiO-66(Ce/Zr).

| Element | Wt.% | At.% |
|---------|-------|-------|
| CK | 44.39 | 68.11 |
| OK | 21.42 | 24.83 |
| ZrL | 17.35 | 4.16 |
| CeL | 16.84 | 2.90 |

The SEM and high-angle annular dark-field imaging (HAADF-STEM) of Cu/UiO-66 materials presented in Figure 5 show that both samples are homogeneous and are composed of small UiO-66 particles that overlap each other. The energy dispersive X-ray spectroscopy (EDS) detected 3.47 and 12.09 wt.% of Cu in Cu/UiO-66(Zr) and Cu/UiO-66(Ce/Zr), respectively. This discrepancy is most probably caused by the inhomogeneous dispersion of copper over UiO-66 particles. Nevertheless, as was also determined with EDS mapping (Figure 6), the Cu dispersion in scanned areas in both samples was very good.

**Figure 5.** Scanning electron microscope (SEM) (up) and STEM (down) images of Cu/UiO-66(Zr) (left) and Cu/UiO-66(Ce/Zr) (right).**Figure 6.** HAADF-STEM images of Cu/UiO-66(Zr), with marked area of Cu and Zr EDS maps (left) and Cu/UiO-66(Ce/Zr), Cu, Ce and Zr EDS maps (right).

The Fourier transform infrared spectroscopy (FT-IR) was used for observations of the surfaces of the obtained UiO-66 and Cu/UiO-66 materials. The FT-IR spectra (Figure 7) of all samples display

bands at the same wavenumber. The presence of vibration mode at 664 and 473 cm^{-1} is due to μ_3 -O and μ_3 -OH stretching vibrations of the $\text{Zr}_6\text{O}_4(\text{OH})_4(\text{CO}_2)_{12}$ in the UiO-66 framework. Whereas the band at 551 cm^{-1} is ascribed to Zr-(OC) asymmetric stretching vibrations. The small band visible at 1507 cm^{-1} in all samples can be associated with the vibration of the C=C in benzene ring in the deprotonated, and thus coordinated, BDC linker. Bands indicating the occurrence of asymmetric and symmetric $\nu(\text{OCO})$ stretchings in the linker are visible at 1578 and 1390 cm^{-1} , respectively. At low frequencies the modes due to OH and CH bending in H_2BDC are mixed with Zr-O modes. Bands at ca. 812, 743, and 714 cm^{-1} correspond to the mix of C-H vibration, C=C stretch, OH bend, and OCO bend in terephthalic acid [33]. The presence of the latter, together with the bands at 1507, 1017 cm^{-1} , can be due to BDC coordination with Zr [34] or Ce nodes. Whereas the presence of free -COOH groups in partially uncoordinated linker is proven by the occurrence of the band at 1673 cm^{-1} . However, that band is not present on the spectra, which implies that obtained in this work UiO-66-based structures are terminated on the surface with Zr and/or Ce clusters. The existence of residual dimethylformamide (DMF) within the pores of obtained UiO-66 and Cu/UiO-66 is normally displayed by the band at 1658 cm^{-1} coming from the C=O asymmetric stretching vibrations. That band is hardly observable on the FT-IR spectra of obtained materials, which indicates successful exchange of solvent after the synthesis of UiO-66(Zr) and UiO-66(Ce/Zr).

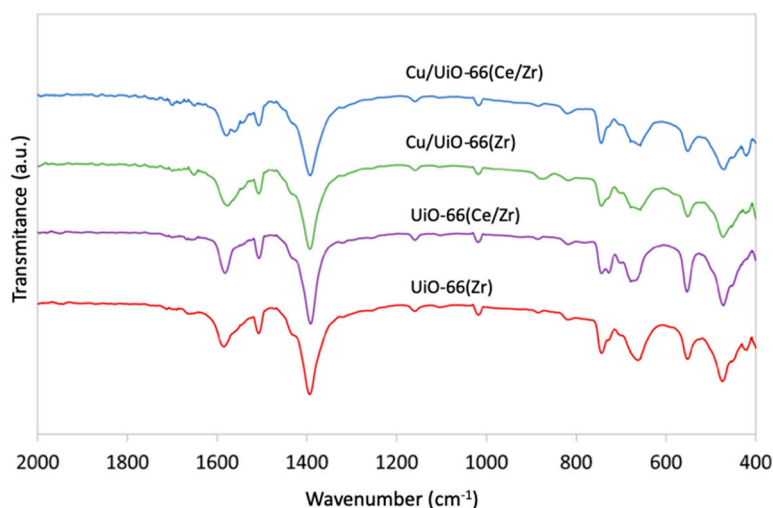


Figure 7. Fourier transform infrared spectroscopy (FT-IR) spectra of UiO-66 and Cu/UiO-66 materials.

Thermal stabilities and the average number of linker defects per one $[\text{Zr}_6\text{O}_4(\text{OH})_4]^{12+}$ cluster in the obtained materials were studied using thermogravimetric analysis (TGA). The low temperature mass decrease with a maximal rate at ca. 100 °C (Figure 8) is as a result of desorption of H_2O from the sample (the FTIR showed that the DMF was successfully removed during solvent exchange step). The H_2O content in the samples, calculated from TGA, increased in the following order: UiO-66(Ce/Zr) < Cu/UiO-66(Ce/Zr) < UiO-66(Zr) < Cu/UiO-66(Zr), being 16.13, 18.21, 19.98, and 23.65%, respectively. Hence, the amount of water was lower for the samples where 50% of Zr^{4+} was replaced with Ce^{4+} , and it slightly increased after impregnation with copper nitrate. Continuous but less significant mass decrease from ca. 120 °C can be due to framework dehydroxylation, i.e., removal of the -OH groups in the form of H_2O from the Zr (or Ce) clusters. Simultaneously, solvent molecules (H_2O and/or DMF—if present) that coordinated with metal clusters to compensate linker deficiencies are removed. The UiO-66(Zr) and UiO-66(Ce/Zr) are thermally stable up to 490 and 450 °C, respectively. Lower thermal resistance of UiO-66(Ce/Zr) compared to UiO-66(Zr) arises from partial exchange of Zr to Ce. The beneficial influence of zirconium on thermal stability of cerium oxide is generally known [35]. As was reported by Lammert et al. [36], increasing amount of Ce in the UiO-66(Ce/Zr) negatively influenced thermal stability of the material, which decreased from 450 °C for UiO-66(Zr) to 220 °C at

40 At.% content of Ce. However, in the present work, the stability of UiO-66(Ce/Zr) with a theoretical Ce/Zr atomic ratio of 1:1 is lower only by 50 °C compared to UiO-66(Zr). As was reported in [36,37] the UiO-66(Ce) was stable only up to 220–240 °C. Also our studies revealed that complete exchange of Zr for Ce in the UiO-66 shifted the temperature of BDC decomposition to ca. 260–280 °C (depending on the synthesis method) which was followed with the collapse of MOF structure [38]. Compared to UiO-66(Zr) and UiO-66(Ce/Zr), a significant decrease in thermal stability, by ca. 150 °C, is observed for their copper-containing analogues. The presence of well dispersed Cu nanoparticles facilitates thermal decomposition of the framework at high temperature by weakening the interaction between -COO^- and Zr^{4+} or Ce^{4+} .

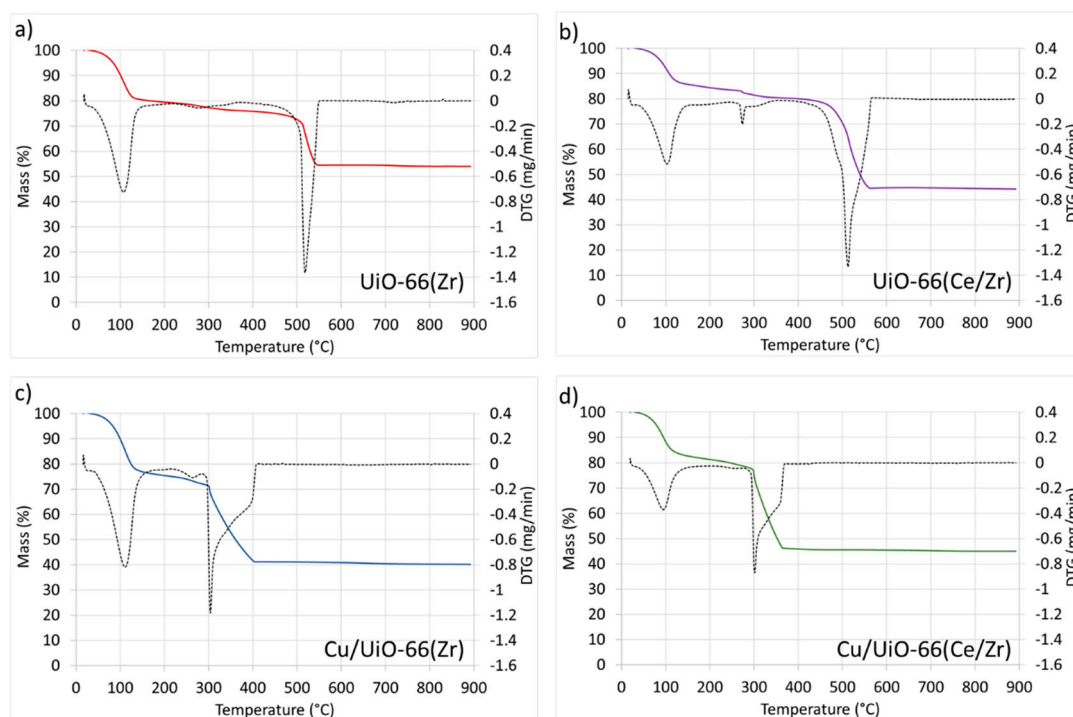


Figure 8. TG (—) and DTG (. . .) for UiO-66 and Cu/UiO-66 materials, **a)** UiO-66(Zr), **b)** UiO-66(Ce/Zr), **c)** Cu/UiO-66(Zr), **d)** Cu/UiO-66(Ce/Zr).

On the basis of TGA we have calculated the average number of linker molecules coordinated to one metal cluster. In an ideal UiO-66 structure to each metal cluster coordinates 12 linker molecules. It can be seen from Table 3 that the amount of linker defects was the highest for UiO-66(Zr) and decreased when half of Zr^{4+} was replaced with Ce^{4+} (i.e., for UiO-66(Ce/Zr)) or when the material was impregnated with copper. Defects in MOFs, either in the linkers or in the metal nodes, are catalytically active sites so their presence is somewhat desired. It is known that the UiO-66 structure remains stable up to 4.3 missing linker molecules per one $[\text{Zr}_6\text{O}_4(\text{OH})_4]^{12+}$ node [39]. Above that number the structure collapses.

Table 3. The amount of linker in the sample and the average number of linker molecules coordinated to one metal cluster—calculated from TGA.

| Sample | Linker (wt.%) | Average Number of Linker Molecules per Metal Cluster |
|------------------|---------------|--|
| UiO-66(Zr) | 49.9 | 11.0 |
| UiO-66(Ce/Zr) | 50.1 | 11.9 |
| Cu/UiO-66(Zr) | 52.9 | 11.6 |
| Cu/UiO-66(Ce/Zr) | 50.0 | 11.9 |

2.2. Catalytic Tests of CO₂ Hydrogenation to MeOH

The results of the catalytic tests of CO₂ hydrogenation to MeOH over the UiO-66(Zr), UiO-66(Ce/Zr), Cu/UiO-66(Zr), and Cu/UiO-66(Ce/Zr) are presented in Figure 9. The MeOH production was changing during first few hours of test run for all catalysts. Selectivity to MeOH over particular catalysts was stable from the third hour of test run (Figure 9b). The gas chromatography (GC) analyses performed during the tests revealed that the only organic by-product of the reaction was dimethyl ether.

According to [18], the adsorption and activation of CO₂ and H₂ takes place on the unsaturated Zr and Cu sites, respectively. But in our conditions the CO₂ activation occurs on the Zr and Ce (if applicable) sites. The poorest selectivity to MeOH, of only 3.5%, was noticed for UiO-66(Zr), but the introduction of cerium to the framework caused significant improvement in that field—selectivity increased to 28.7%. However, the introduction of Ce to the UiO-66 does not influence the rate of MeOH synthesis, which was found to be 278 $\mu\text{mol}_{\text{MeOH}}/\text{g}_{\text{Cu}}/\text{h}$ for UiO-66(Zr) and 275 $\mu\text{mol}_{\text{MeOH}}/\text{g}_{\text{Cu}}/\text{h}$ for UiO-66(Ce/Zr). The best performance in catalytic CO₂ hydrogenation showed the Cu-loaded materials. The methanol STY after 25 h of test run was 468 $\mu\text{mol}_{\text{MeOH}}/\text{g}_{\text{Cu}}/\text{h}$ for Cu/UiO-66(Ce/Zr) and 397 $\mu\text{mol}_{\text{MeOH}}/\text{g}_{\text{Cu}}/\text{h}$ for Cu/UiO-66(Zr), whereas the selectivity to MeOH reached 59 and 56%, respectively (Figure 10). Our results are much better than those reported by Kobayashi et al. [19] who obtained 67.8 and 114.2 $\mu\text{mol}_{\text{MeOH}}/\text{g}_{\text{Cu}}/\text{h}$ over UiO-66(Zr) and Cu/UiO-66(Zr), respectively—over 4 times less than for corresponding catalysts discussed in this work. Nevertheless, obtained in their work Cu/UiO-66(Zr) revealed over 90% selectivity to MeOH, which is much better than that compared to our work. It must be also mentioned here, that they performed the catalytic test at higher T and lower pressure than we did (T = 220 °C, p = 2 Atm., H₂/CO₂ of 5:1). Those condition could have an impact on the catalysts performance since the reaction favours lower temperature and higher pressure.

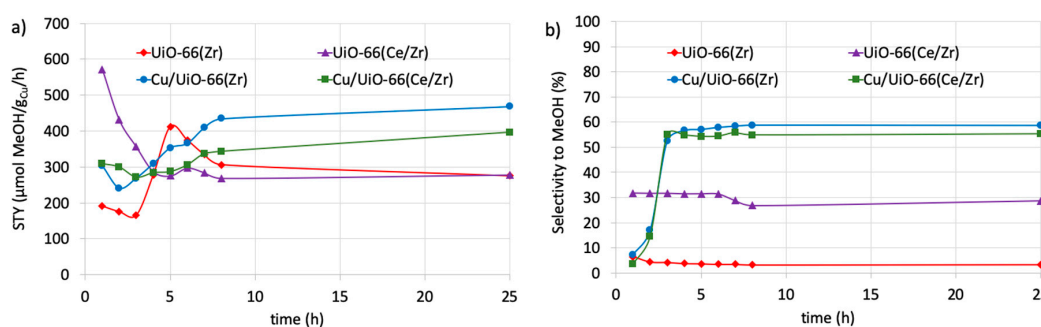


Figure 9. Space time yield (a) and MeOH selectivity (b) during catalytic tests of CO₂ hydrogenation over UiO-66 and Cu/UiO-66 materials (T = 200 °C, p = 18 bar, H₂/CO₂ = 3:1).

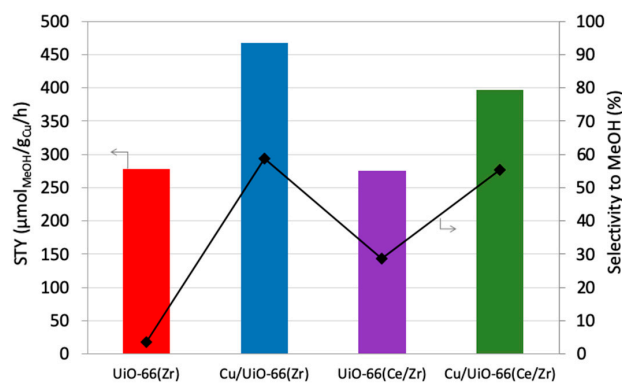


Figure 10. Selectivity to MeOH and space time yield over UiO-66 and Cu/UiO-66 materials after 25 h of catalytic tests.

We have anticipated that Ce introduction to the Cu/Uio-66(Zr) would improve its performance, but unlike it was expected, the MeOH production over Cu/Uio-66(Ce/Zr) was lower than for Cu/Uio-66(Zr) (Figure 10). The Cu-containing catalysts were pre-reduced in H₂/Ar prior to the tests to provide Cu⁰ active sites for H₂ dissociation, but CuO reduction might have not been completed and except for Cu⁰, the cationic copper (e.g. Cu₂O) could have been also present on the catalyst surface [38]. It is known that the combination of Cu species plays important role in the catalyst performance: the Cu⁰ is responsible for H₂ dissociation, whereas Cu⁺ stabilizes the formate intermediates. We expect that the decrease in MeOH production in the case of Cu/Uio-66(Ce/Zr) (when compared to Cu/Uio-66(Zr)), can be due to strong interaction between Cu⁰ and Ce⁴⁺ cluster that facilitates the oxygen spill-over from Ce⁴⁺ to Cu⁰, destabilizing (i.e., oxidizing) the active site for H₂ adsorption and dissociation. It was found by the HAADF-STEM with the EDS elemental mapping, that copper was well-dispersed in Cu/Uio-66(Zr) and Cu/Uio-66(Ce/Zr) samples. It is known, that the formation of nanostructured copper-ceria composites characterizes with the strong electronic interactions between nanoparticles [40], and the transition between Ce³⁺ and Ce⁴⁺ takes place by the equilibration of mobile oxygen vacancies at the Cu–Ce interface [41]. In the presented case, that strong Cu–Ce interaction can be also proven by the significant decrease in thermal stability of Cu/Uio-66(Ce/Zr) compared to Uio-66(Ce/Zr) (Figure 8). Such a strong Cu⁰ and Ce⁴⁺ interaction can significantly inhibit the MeOH formation because H₂ dissociation is required for hydrogenation of the surface formate, which is the rate determining step. From the other hand, zirconium is non-reducible and stabilizes Cu⁰ active sites. We may assume that Cu/Uio-66(Zr) possess more Cu⁰ active sites than Cu/Uio-66(Ce/Zr).

Also, different character of Cu-Zr and Cu-Ce interactions explains the difference in MeOH selectivity on Cu/Uio-66(Zr) and Cu/Uio-66(Ce/Zr). On those catalysts the reaction takes place at the Cu-Zr⁴⁺ and the Cu-Zr⁴⁺ / Cu-Ce⁴⁺ interfaces. But the mechanism of CO₂ hydrogenation to MeOH is different for Zr- and Ce-containing systems, which results in different product selectivity. It was found by Wang et al. [42] that CO₂ adsorption on Cu-ZrO₂ promotes formation of bicarbonate species that are later hydrogenated to hydrocarboxyl species (COOH), and those readily decompose to CO, which decreases MeOH selectivity. Whereas the Cu-CeO₂ assists formation of surface carbonates that are first hydrogenated to formate species (HOOC) and further hydrogenated to MeOH. However, our results show that the presence of cerium in Cu/Uio-66(Ce/Zr) does not improve MeOH selectivity compared to Cu/Uio-66(Zr).

Considering the effect of the concentration of structure defects in Uio-66 on its performance in MeOH synthesis via CO₂ hydrogenation, it was noticed (likewise reported in [19]) that there is no correlation between those two parameters. Rungtaweeworanit et al. [9] observed that the most important is Cu contact with the support. By encapsulation of copper inside the Uio-66 framework they increased the MeOH production, when compared to Cu deposited over Uio-66. It was explained with higher number of active Cu sites surrounded by the Zr oxide SBU in the case of metal encapsulation, and thus, strong metal-support interaction.

2.3. Characterization After Catalytic Tests

The XRD analyses of spent catalyst (Figure 11) exhibited that their crystal structures changed after reaction carried out under increased pressure (1.8 MPa) and temperature (200 °C) for 25 h. It can be seen that cerium insertion into the Uio-66 framework stabilizes it to some extent (vide two characteristic reflexions at $2\theta = 7.38$ and 8.52° on the diffractograms of Uio-66(Ce/Zr) and Cu/Uio-66(Ce/Zr), corresponding to (111) and (200) planes in Uio-66). The diffractograms of Uio-66(Zr) and Uio-66(Ce/Zr) also display the symmetry forbidden (110) reflection at $2\theta = 6.57^\circ$ that indicates the presence of the **reo** unit cell, which is equivalent to missing an entire Zr₆O₆(BDC)₁₂¹²⁻ SBU; thus, the existence of open Zr centers. In such a case, the unit cell has a 12+ net positive charge that has to be compensated by negatively charged ligands [43]. Cliffe et al. [44] reported that this charge can be compensated by formate. The presence of reflexions at $2\theta = 6.57^\circ$, ascribed to coordination deficiencies in the Uio-66(Zr) and Uio-66(Ce/Zr), can be caused by the reaction conditions, i.e., increased p, T, and the duration of the

catalytic test. Moreover, the reflexions of Cu (111) are visible for Cu/UiO-66(Zr) and Cu/UiO-66(Ce/Zr) at $2\theta = 43.3^\circ$. Reflexion coming from Cu species were not present on the diffractograms of fresh catalysts; hence, their detection by the XRD after tests can be caused by Cu agglomeration. Also, if the MOF structure was partially destroyed, the concentration of Cu in the sample increased. The changes in the samples structures after catalytic tests influenced their textural properties, i.e., the S_{BET} of all samples decreased and the mean pore size increased (Table 4). The most significant deterioration of textural properties can be observed for UiO-66(Zr).

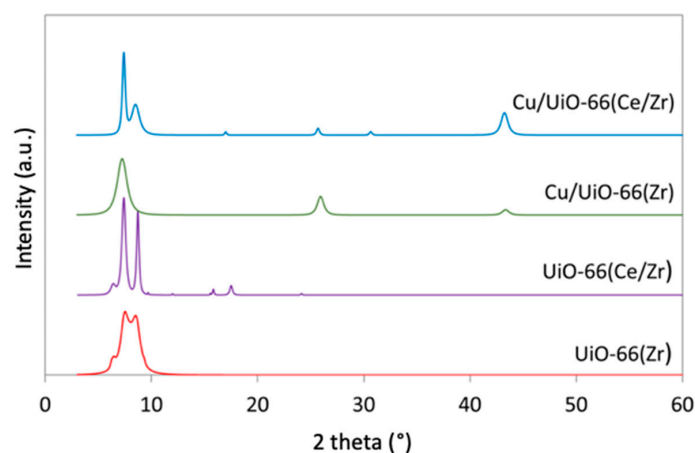


Figure 11. XRD of UiO-66 and Cu/UiO-66 materials after MeOH synthesis.

Table 4. Textural properties of UiO-66 and Cu/UiO-66 after MeOH synthesis.

| SAMPLE | S_{BET} (m^2/g) | V_{total} (cm^3/g) | d (\AA) |
|------------------|--|---|----------------------|
| UiO-66(Zr) | 34 | 0.026 | 306 |
| UiO-66(Ce/Zr) | 345 | 0.363 | 42.0 |
| Cu/UiO-66(Zr) | 217 | 0.260 | 34.9 |
| Cu/UiO-66(Ce/Zr) | 149 | 0.130 | 47.9 |

The FT-IR spectra of spent catalyst are presented in Figure 12. The decrease of intensities of bands at 664 , 473 , and 551 cm^{-1} corresponding to $\mu_3\text{-O}$, $\mu_3\text{-OH}$, and Zr-OC in the $\text{Zr}_6\text{O}_4(\text{OH})_4(\text{CO}_2)_{12}$ SBU is observed. It implies some degradation of the $[\text{Zr}_6\text{O}_4(\text{OH})_4]$ clusters caused by the extended reaction at elevated pressure and temperature. It can be associated to the formation of the whole cluster defects and the **reo** unit cell that was previously detected with the XRD (Figure 11). The existence of coordinated BDC linker in the UiO-66 is proven by the bands at 1507 and 744 cm^{-1} associated with the vibration of the $\text{C}=\text{C}$ in benzene ring, and bands at $1550\text{--}1650 \text{ cm}^{-1}$ and $1335\text{--}1446 \text{ cm}^{-1}$ regions corresponding to asymmetric and symmetric $\nu(\text{OCO})_{\text{as}}$ stretching vibrations.

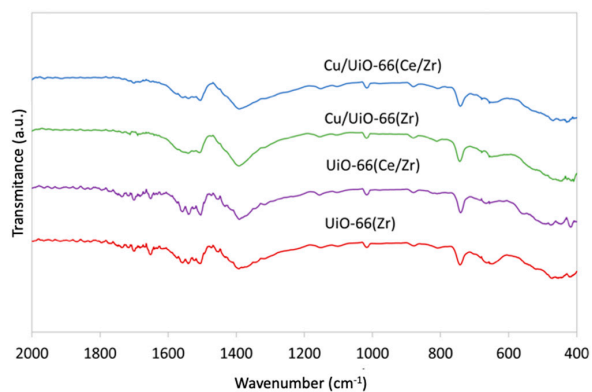


Figure 12. FT-IR of UiO-66 and Cu/UiO-66 materials after catalytic tests of MeOH synthesis.

3. Materials and Methods

3.1. Synthesis of UiO-66 and UiO-66(Ce/Zr)

The UiO-66(Zr) was synthesized according to the procedure described by Katz et al. [45]. In the first flask, 1 g of zirconium (IV) chloride was dissolved in 40 mL of DMF. Next, 8 mL of concentrated HCl was added. In the second flask 0.984 g of terephthalic acid (H₂BDC) was dissolved in 80 mL of DMF. Both solutions were poured into the Teflon-lined autoclave, mixed together for 30 min and heated at 80 °C for 24 h. The obtained white product was filtered under reduced pressure and washed three times with 40 mL of DMF. Then the powder was suspended in 100 mL of ethanol for three days in order to exchange the residual DMF to EtOH. In the final step the product was filtered again and dried at 80 °C for 12 h. All the chemicals were purchased from Sigma Aldrich.

The bimetallic UiO-66(Ce/Zr) was obtained by dissolving 1.73 g of ammonium cerium (IV) nitrate and 0.74 g of zirconium (IV) chloride in 15 mL DMF and mixed together for 20 min. The solution of organic linker was prepared by dissolving 1 g of H₂BDC in 68 mL of DMF under continuous stirring for 30 min. Both the solutions were transferred to Teflon-lined autoclave and heated at 120 °C for 48 h. Obtained yellowish white product was filtered, washed with 40 mL of DMF, and suspended in 100 mL of ethanol for three days. After DMF to EtOH exchange the powder was filtered again and dried at 80 °C for 12 h.

3.2. Synthesis of Cu/UiO-66

The Cu/UiO-66(Zr) and Cu/UiO-66(Ce/Zr), with the nominal loading of Cu of 10 wt.%, were obtained via the incipient wetness impregnation (IWI) method. The ethanolic solution of copper nitrate trihydrate solution was slowly instilled into the flasks with UiO-66(Zr) or UiO-66(Ce/Zr) powders and stirred continuously. Obtained green powders were left overnight at room temperature to dry slowly and then heated at 160 °C for 12 h.

3.3. Characterization

The N₂ adsorption–desorption experiments were carried out using the Autosorb 1C apparatus (Quantachrome Instruments, Boynton Beach, FL, USA) at 77 K. Before measurements the samples were outgassed in vacuum at 100 °C for 12 h. The specific surface areas (S_{BET}) were determined using the multipoint BET method. The specific total pore volume was evaluated from the N₂ uptake at a relative pressure of $P/P_0 = 0.99$.

The powder X-ray diffraction (XRD) was conducted using the X'Pert Pro apparatus (PANalytical, Malvern, UK) using Ni-filtered Cu K α radiation ($\lambda = 1.54056 \text{ \AA}$) equipped with specific optics to perform analysis by small-angle X-ray scattering (SAXS) in transmission geometry) with X'Pert HighScore Plus program used for display and analysis of the diffraction patterns. The scanning was performed from 5 to 80° with a rate of 0.03°/step.

The powder X-ray diffraction (XRD) was conducted using the X'Pert Pro apparatus (PANalytical, Malvern, UK) using Ni-filtered Cu K α radiation ($\lambda = 1.54056 \text{ \AA}$) equipped with specific optics to perform analysis by small-angle X-ray scattering (SAXS) in transmission geometry) with X'Pert HighScore Plus program used for display and analysis of the diffraction patterns. The scanning was performed from 5 to 80° with a rate of 0.03°/step.

The thermogravimetric analysis (TGA) of the catalyst was performed using Autosorb iQ apparatus (Quantachrome, Boynton Beach, FL, USA). The change of sample mass was registered under flowing air at temperature increasing from 25 to 900 °C with a 10 °C/min heating rate.

The X-ray photoelectron spectroscopy (XPS) was performed using a Thermo-Scientific K-ALPHA spectrometer (Waltham, MA, USA) equipped in Al-K radiation (1486.6 eV) monochromatized by a twin crystal monochromator, yielding a focused X-ray spot with a diameter of 400 μm , at 3 mA \times 12 kV when charge compensation was achieved with the system flood gun that provides low energy electrons and low energy argon ions from a single source. The alpha hemispherical analyser was operated in

the constant energy mode with survey scan pass energies of 200 eV to measure the whole energy band, and 50 eV in a narrow scan to selectively measure the particular elements. An estimation of the intensities was done after a calculation of each peak integral. S-shaped background subtraction and fitting the experimental curve to a combination of a Lorentzian (30%) and Gaussian (70%) lines. Binding energies, referenced to the C1s line at 284.6 eV, have an accuracy of ± 0.1 eV.

The microscopic observations of the samples were carried out using scanning electron microscope (SEM, Zeiss Supra 35, Zeiss, Oberkochen, Germany) with field emission gun, equipped with TEAMTM Trident Analysis system. The secondary electron imaging and energy-dispersive X-ray spectroscopy (EDX) were used to determine the morphology of the analyzed materials. The transmission electron microscopy (TEM) was performed using Cs-corrected transmission electron microscope S/TEM Titan 80-300 (FEI), operating at an accelerating voltage of 300 kV, and equipped with Schottky-type field emission gun, CETCOR Cs-probe corrector (CEOS, Heidelberg, Germany), a Gatan Energy Filter (Tridiem 863, Cambridge, UK) and EDS detector. The scanning transmission electron microscopy (STEM) and high-resolution transmission electron microscopy (HRTEM) imaging were applied as primary research techniques. The chemical composition of studied samples was examined with energy dispersive spectrometry (EDS).

3.4. Catalytic Tests

The activity tests of synthesised UiO-66 and Cu/UiO-66 materials were performed in a non-gradient reactor of a 300 cm³ volume using a H₂/CO₂ mixture of a 3:1 ratio and a flow rate of 80 mL/min. The tests were carried out at 200 °C and $p = 1.8$ MPa. For each test, a catalyst sample of 0.2 g was used. The concentration of reagents at the reactor outlet was measured by gas chromatography throughout the experiment that lasted 25 h.

4. Conclusions

In this work the UiO-66 and Cu/UiO-66 materials were obtained, characterized and tested in CO₂ hydrogenation to methanol. An approach to exchange half of Zr⁴⁺ cations with Ce⁴⁺ in the UiO-66 framework was made. The impact of Ce and Cu presence in the UiO-66-based catalytic system on the methanol production and selectivity to methanol was determined.

All of obtained materials were crystalline and possessed developed surface area; however, some decrease in S_{BET} was noticed after Ce introduction to the UiO-66 framework and after copper deposition. As was proven by the XPS and STEM/EDS, the concentration of cerium in UiO-66(Ce/Zr) was lower than assumed, i.e., less than 50% of Zr was replaced with Ce. Moreover, the dispersion of Ce in the UiO-66 framework was uniform. In the obtained UiO-66(Ce/Zr) and Cu/UiO-66(Ce/Zr) samples cerium occurred in its +4 and +3 oxidation state, but the former predominated. The EDS elemental mapping indicated good Cu dispersion over the UiO-66(Zr) and UiO-(Ce/Zr) samples. Strong Cu-Zr and Cu-Ce interactions caused significant decrease in thermal stability of the UiO-66(Zr) and UiO-66(Ce/Zr) samples. Besides, strong Cu-Ce interaction in Cu/UiO-66(Ce/Zr) facilitated oxygen transfer at the Cu⁺-Ce⁴⁺ interface, resulting in the reduction of Ce⁴⁺ to Ce³⁺ and oxidation of Cu⁺ to Cu²⁺.

The composition of UiO-66-based catalytic system, especially the character of Cu-Zr and Cu-Ce interactions, had an impact on MeOH production and MeOH selectivity. The partial exchange of Zr with Ce in UiO-66 did not influence the MeOH production but significantly increased the selectivity to MeOH. It was due to the formation of surface carbonates during CO₂ adsorption on Ce sites, and their further hydrogenation first to formate species, and finally, to methanol. The CO₂ hydrogenation over Zr nodes in UiO-66(Zr) was occurring with the formation of surface bicarbonates whose hydrogenation to hydrocarboxyl species is followed with CO formation that decreases MeOH selectivity. The above phenomena did not apply in the case of the Cu/UiO-66 catalytic systems, i.e., the selectivity to MeOH was very similar for both Cu/UiO-66(Zr) and Cu/UiO-66(Ce/Zr). In addition, the former showed higher MeOH production. Both catalysts suffered from some degradation of the structure after catalytic tests. The defects formed under reaction conditions because of degradation of [Zr₆O₄(OH)₄] clusters.

It caused the decrease in the S_{BET} and the increase of pore size. Moreover, partial destruction of UiO-66 framework led to agglomeration of copper.

Author Contributions: Conceptualization, A.Ł. and M.S.; methodology, A.Ł. and M.S.; investigation, M.S., R.C., R.Ł. and K.M.; resources, J.T., T.M. and J.S.-A.; writing—original draft preparation, A.Ł., M.S.; writing—review and editing, A.Ł.; supervision, A.Ł., J.T.; funding acquisition, M.S. and J.T. All authors have read and agreed to the published version of the manuscript.

Acknowledgments: This work was financed by a statutory activity subsidy from the Polish Ministry of Science and Higher Education for the Faculty of Chemistry of Wrocław University of Technology and the project 0402/0100/17.

Conflicts of Interest: The authors declare no conflict of interest.

References

1. Li, C.-S.; Melaet, G.; Ralston, W.T.; An, K.; Brooks, C.; Ye, Y.; Liu, Y.-S.; Zhu, J.; Guo, J.; Alayoglu, S.; et al. High-performance hybrid oxide catalyst of manganese and cobalt for low-pressure methanol synthesis. *Nat. Commun.* **2015**, *6*, 6538. [[CrossRef](#)] [[PubMed](#)]
2. Studt, F.; Abild-Pedersen, F.; Wu, Q.; Jensen, A.D.; Temel, B.; Grunwaldt, J.-D.; Nørskov, J.K. CO hydrogenation to methanol on Cu–Ni catalysts: Theory and experiment. *J. Catal.* **2012**, *293*, 51–60. [[CrossRef](#)]
3. Schumann, J.; Lunkenbein, T.; Tarasov, A.; Thomas, N.; Schlögl, R.; Behrens, M. Synthesis and Characterisation of a Highly Active Cu/ZnO:Al Catalyst. *ChemCatChem* **2014**, *6*, 2889–2897. [[CrossRef](#)]
4. Sayah, A.K.; Hosseinabadi, S.; Farazar, M. CO₂ abatement by methanol production from flue-gas in methanol plant. *World Acad. Sci. Eng. Technol. Int. J. Chem. Mol. Eng.* **2010**, *4*, 9. [[CrossRef](#)]
5. Jadhav, S.G.; Vaidya, P.D.; Bhanage, B.M.; Joshi, J.B. Catalytic carbon dioxide hydrogenation to methanol: A review of recent studies. *Chem. Eng. Res. Des.* **2014**, *92*, 2557–2567. [[CrossRef](#)]
6. Behrens, M.; Studt, F.; Kasatkin, I.; Kühl, S.; Hävecker, M.; Abild-Pedersen, F.; Zander, S.; Girgsdies, F.; Kurr, P.; Knief, B.-L.; et al. The Active Site of Methanol Synthesis over Cu/ZnO/Al₂O₃ Industrial Catalysts. *Science* **2012**, *336*, 893. [[CrossRef](#)]
7. Inui, T.; Takeguchi, T. Effective conversion of carbon dioxide and hydrogen to hydrocarbons. *Catal. Today* **1991**, *10*, 95–106. [[CrossRef](#)]
8. Naims, H. Economics of carbon dioxide capture and utilization – a supply and demand perspective. *Environ. Sci. Pollut. Res.* **2016**, *23*, 22226–22241. [[CrossRef](#)]
9. Rungtaweeveranit, B.; Baek, J.; Araujo, J.R.; Archanjo, B.S.; Choi, K.M.; Yaghi, O.M.; Somorjai, G.A. Copper Nanocrystals Encapsulated in Zr-based Metal–Organic Frameworks for Highly Selective CO₂ Hydrogenation to Methanol. *Nano Lett.* **2016**, *16*, 7645–7649. [[CrossRef](#)]
10. Klier, K. Catalytic synthesis of methanol from CO/H₂. The effects of carbon dioxide. *J. Catal.* **1982**, *74*, 343–360. [[CrossRef](#)]
11. Jeong, C.; Suh, Y.-W. Role of ZrO₂ in Cu/ZnO/ZrO₂ catalysts prepared from the precipitated Cu/Zn/Zr precursors. *Catal. Today* **2016**, *265*, 254–263. [[CrossRef](#)]
12. Li, C.; Yuan, X.; Fujimoto, K. Development of highly stable catalyst for methanol synthesis from carbon dioxide. *Appl. Catal. A: Gen.* **2014**, *469*, 306–311. [[CrossRef](#)]
13. Sloczyński, J.; Grabowski, R.; Kozłowska, A.; Olszewski, P.; Lachowska, M.; Skrzypek, J.; Stoch, J. Effect of Mg and Mn oxide additions on structural and adsorptive properties of Cu/ZnO/ZrO₂ catalysts for the methanol synthesis from CO₂. *Appl. Catal.* **2013**, *249*, 129–138. [[CrossRef](#)]
14. Liang, X.-L.; Dong, X.; Lin, G.-D.; Zhang, H.-B. Carbon nanotube-supported Pd–ZnO catalyst for hydrogenation of CO₂ to methanol. *Appl. Catal. B* **2009**, *88*, 315–322. [[CrossRef](#)]
15. Deerattrakul, V.; Dittanet, P.; Sawangphruk, M.; Kongkachuichay, P. CO₂ hydrogenation to methanol using Cu–Zn catalyst supported on reduced graphene oxide nanosheets. *J. CO₂ Util.* **2016**, *16*, 104–113. [[CrossRef](#)]
16. Graciani, J.; Mudiyansele, K.; Xu, F.; Baber, A.E.; Evans, J.; Senanayake, S.D.; Stacchiola, D.J.; Liu, P.; Hrbek, J.; Fernández Sanz, J.; et al. Highly active copper-ceria and copper-ceria-titania catalysts for methanol synthesis from CO₂. *Science* **2014**, *345*, 546–550. [[CrossRef](#)]
17. Allam, D.; Bennici, S.; Limousy, L.; Hocine, S. Improved Cu- and Zn-based catalysts for CO₂ hydrogenation to methanol. *Cr. Chim.* **2019**, *22*, 227–237. [[CrossRef](#)]

18. An, B.; Zhang, J.; Cheng, K.; Ji, P.; Wang, C.; Lin, W. Confinement of Ultrasmall Cu/ZnOx Nanoparticles in Metal–Organic Frameworks for Selective Methanol Synthesis from Catalytic Hydrogenation of CO₂. *J. Am. Chem. Soc.* **2017**, *139*, 3834–3840. [[CrossRef](#)]
19. Kobayashi, H.; Taylor, J.M.; Mitsuka, Y.; Ogiwara, N.; Yamamoto, T.; Toriyama, T.; Matsumura, S.; Kitagawa, H. Charge transfer dependence on CO₂ hydrogenation activity to methanol in Cu nanoparticles covered with metal–organic framework systems. *Chem. Sci.* **2019**, *10*, 3289–3294. [[CrossRef](#)]
20. Cavka, J.H.; Jakobsen, S.; Olsbye, U.; Guillou, N.; Lamberti, C.; Bordiga, S.; Lillerud, K.P. A New Zirconium Inorganic Building Brick Forming Metal Organic Frameworks with Exceptional Stability. *J. Am. Chem. Soc.* **2008**, *130*, 13850–13851. [[CrossRef](#)]
21. Biswas, S.; Van Der Voort, P. A General Strategy for the Synthesis of Functionalised UiO-66 Frameworks: Characterisation, Stability and CO₂ Adsorption Properties. *Eur. J. Inorg. Chem.* **2013**, *12*, 2154–2160. [[CrossRef](#)]
22. Furukawa, H.; Gándara, F.; Zhang, Y.B.; Jiang, J.; Queen, W.L.; Hudson, M.R.; Yaghi, O.M. Water Adsorption in Porous Metal–Organic Frameworks and Related Materials. *J. Am. Chem. Soc.* **2014**, *136*, 4369–4381. [[CrossRef](#)] [[PubMed](#)]
23. De Coste, J.B.; Peterson, G.W.; Jasuja, H.; Glover, T.G.; Huang, Y.; Walton, K.S. Stability and degradation mechanisms of metal–organic frameworks containing the Zr₆O₄(OH)₄ secondary building unit. *J. Mater. Chem. A* **2013**, *1*, 5642–5650. [[CrossRef](#)]
24. Zhou, F.; Lu, N.; Fan, B.; Wang, H.; Li, R. Zirconium-containing UiO-66 as an efficient and reusable catalyst for transesterification of triglyceride with methanol. *J. Energy Chem.* **2016**, *25*, 874–879. [[CrossRef](#)]
25. Limvorapitux, R.; Chen, H.; Mendonca, M.; Liu, M.; Snurr, R.Q.; Nguyen, S.T. Elucidating the mechanism of the UiO-66-catalyzed sulfide oxidation: Activity and selectivity enhancements through changes in the node coordination environment and solvent. *Catal. Sci. Technol.* **2019**, *9*, 327–335. [[CrossRef](#)]
26. Viana, A.M.; Ribeiro, S.O.; Castro, B.; Balula, S.S.; Cunha-Silva, L. Influence of UiO-66(Zr) Preparation Strategies in Its Catalytic Efficiency for Desulfurization Process. *Materials* **2019**, *12*, 3009. [[CrossRef](#)]
27. Dhakshinamoorthy, A.; Santiago-Portillo, A.; Asiri, A.M.; García, H. Engineering UiO-66 Metal Organic Framework for Heterogeneous Catalysis. *ChemCatChem.* **2019**, *11*, 899–923. [[CrossRef](#)]
28. Wang, J.-C.; Hu, Y.-H.; Chen, G.-J.; Dong, Y.-B. Cu(ii)/Cu(0)@UiO-66-NH₂: Base metal@MOFs as heterogeneous catalysts for olefin oxidation and reduction. *Chem. Commun.* **2016**, *52*, 13116–13119. [[CrossRef](#)]
29. Øien, S.; Wragg, D.; Reinsch, H.; Svelle, S.; Bordiga, S.; Lamberti, C.; Lillerud, K.P. Detailed structure analysis of atomic positions and defects in zirconium metal–organic frameworks. *Cryst. Growth Des.* **2014**, *14*, 5370–5372. [[CrossRef](#)]
30. Shannon, R. Revised effective ionic radii and systematic studies of interatomic distances in halides and chalcogenides. *Acta Cryst. Sect. A* **1976**, *32*, 751–767. [[CrossRef](#)]
31. Peng, B.; Feng, C.; Liu, S.; Zhang, R. Synthesis of CuO catalyst derived from HKUST-1 temple for the low-temperature NH₃-SCR process. *Catal. Today* **2018**, *314*, 122–128. [[CrossRef](#)]
32. Kettner, M.; Ševčíková, K.; Homola, P.; Matolín, V.; Nežasil, V. Influence of the Ce–F interaction on cerium photoelectron spectra in CeO_xF_y layers. *Chem. Phys. Lett.* **2015**, *639*, 126–130. [[CrossRef](#)]
33. Valenzano, L.; Civalleri, B.; Chavan, S.; Bordiga, S.; Nilsen, M.H.; Jakobsen, S.; Lillerud, K.P.; Lamberti, C. Disclosing the Complex Structure of UiO-66 Metal Organic Framework: A Synergic Combination of Experiment and Theory. *Chem. Mater.* **2011**, *23*, 1700–1718. [[CrossRef](#)]
34. Vellingiri, K.; Kumar, P.; Deep, A.; Kim, K.-H. Metal-organic frameworks for the adsorption of gaseous toluene under ambient temperature and pressure. *Chem. Eng. J.* **2017**, *307*, 1116–1126. [[CrossRef](#)]
35. Strandwitz, N.C.; Shaner, S.; Stucky, G.D. Compositional tunability and high temperature stability of ceria–zirconia hollow spheres. *J. Mater. Chem.* **2011**, *21*, 10672. [[CrossRef](#)]
36. Lammert, M.; Glißmann, C.; Reinsch, H.; Stock, N. Synthesis and Characterization of New Ce(IV)-MOFs Exhibiting Various Framework Topologies. *Cryst. Growth Des.* **2017**, *17*, 1125–1131. [[CrossRef](#)]
37. Lammert, M.; Wharmby, M.T.; Smolders, S.; Bueken, B.; Lieb, A.; Lomachenko, K.A.; Vos, D.D.; Stock, N. Cerium-based metal organic frameworks with UiO-66 architecture. *Chem. Commun.* **2015**, *51*, 12578–12581. [[CrossRef](#)]

38. Stawowy, M.; Rózewicz, M.; Szczepańska, E.; Silvestre-Albero, J.; Zawadzki, M.; Musioł, M.; Łuzny, R.; Kaczmarczyk, J.; Trawczyński, J.; Łamacz, A. The Impact of Synthesis Method on the Properties and CO₂ Sorption Capacity of UiO-66(Ce). *Catalysts* **2019**, *9*, 309. [[CrossRef](#)]
39. Bueken, B.; Van Velthoven, N.; Krajnc, A.; Smolders, S.; Taulelle, F.; Mellot-Draznieks, C.; Mali, G.; Bennett, T.D.; De Vos, D. Tackling the Defect Conundrum in UiO-66: A Mixed-Linker Approach to Engineering Missing Linker Defects. *Chem. Mater.* **2017**, *29*, 10478–10486. [[CrossRef](#)]
40. Konsolakis, M. The role of Copper–Ceria interactions in catalysis science: Recent theoretical and experimental advances. *Appl. Catal. B: Environ.* **2016**, *198*, 49–66. [[CrossRef](#)]
41. Duchoň, T.; Dvořák, F.; Aulická, M.; Stetsovych, V.; Vorokhta, M.; Mazur, D.; Veltruska, K.; Skala, T.; Myslivecek, J.; Matolinova, I.; et al. Ordered Phases of Reduced Ceria As Epitaxial Films on Cu(111). *J. Phys. Chem. C* **2013**, *118*, 357–365. [[CrossRef](#)]
42. Wang, W.; Qu, Z.; Song, L.; Fu, Q. CO₂ hydrogenation to methanol over Cu/CeO₂ and Cu/ZrO₂ catalysts: Tuning methanol selectivity via metal-support interaction. *J. Energ. Chem.* **2020**, *40*, 22–30. [[CrossRef](#)]
43. Shearer, G.C.; Chavan, S.; Bordiga, S.; Svelle, S.; Olsbye, U.; Lillerud, K.P. Defect Engineering: Tuning the Porosity and Composition of the Metal–Organic Framework UiO-66 via Modulated Synthesis. *Chem. Mater.* **2016**, *28*, 3749–3761. [[CrossRef](#)]
44. Cliffe, M.J.; Wan, W.; Zou, X.; Chater, P.A.; Kleppe, A.K.; Tucker, M.G.; Wilhelm, H.; Funnell, N.P.; Coudert, F.-X.; Goodwin, A.L. Correlated defect nanoregions in a metal-organic framework. *Nat. Commun.* **2014**, *5*, 4176. [[CrossRef](#)] [[PubMed](#)]
45. Katz, M.J.; Brown, Z.J.; Colón, Y.J.; Siu, P.W.; Scheidt, K.A.; Snurr, R.Q.; Hupp, J.T.; Farha, O.K. A facile synthesis of UiO-66, UiO-67 and their derivatives. *Chem. Commun.* **2013**, *49*, 9449. [[CrossRef](#)] [[PubMed](#)]



© 2019 by the authors. Licensee MDPI, Basel, Switzerland. This article is an open access article distributed under the terms and conditions of the Creative Commons Attribution (CC BY) license (<http://creativecommons.org/licenses/by/4.0/>).